Direct numerical simulation and the theory of receptivity in a hypersonic boundary layer

Anatoli Tumin
The University of Arizona, Tucson, Arizona 85721

Xiaowen Wang and Xiaolin Zhong
The University of California, Los Angeles, California 90095

(Received 3 September 2006; accepted 10 November 2006; published online 5 January 2007)

Direct numerical simulation of receptivity in a boundary layer over a sharp wedge of half-angle 5.3 degrees is carried out with two-dimensional perturbations introduced into the flow by periodic-in-time blowing-suction through a slot. The freestream Mach number is equal to 8. The perturbation flow field downstream from the slot is decomposed into normal modes with the help of the biorthogonal eigenfunction system. Filtered-out amplitudes of two discrete normal modes and of the fast acoustic modes are compared with the linear receptivity problem solution. The examples illustrate how the multimode decomposition technique may serve as a tool for gaining insight into computational results. © *2007 American Institute of Physics*. [DOI: 10.1063/1.2409731]

I. INTRODUCTION

The progress being made in computational fluid dynamics provides an opportunity for reliable simulation of such complex phenomena as laminar-turbulent transition. The dynamics of flow transition depends on the instability of small perturbations excited by external sources. Computational results provide complete information about the flow field that would be impossible to measure in real experiments. However, validation of the results might be a challenging problem. Sometimes, numerical simulations of small perturbations in boundary layers are accompanied by comparisons with results obtained within the scope of the linear stability theory. In principle, this is possible in the case of a flow possessing an unstable mode. Far downstream from the actuator, the perturbations might be dominated by the unstable mode, and one may compare the computational results for the velocity and temperature perturbation profiles and their growth rates with the linear stability theory. This analysis does not work when the amplitude of the unstable mode is comparable to that of other modes, or when one needs to evaluate the amplitude of a decaying mode.

Recently, a method of normal mode decomposition was developed for two- and three-dimensional perturbations in compressible and incompressible boundary layers.[1–3] The method is based on the expansion of solutions of linearized Navier-Stokes equations for perturbations of prescribed frequency into the normal modes of discrete and continuous spectra. The instability modes belong to the discrete spectrum, whereas the continuous spectrum is associated with vorticity, entropy, and acoustic modes. Because the problem of perturbations within the scope of the linearized Navier-Stokes equations is not self-adjoint, the eigenfunctions representing the normal modes are not orthogonal. Therefore, the eigenfunctions of the adjoint problem are involved in the computation of the normal modes' weights.

Originally, the method based on the expansion into the normal modes was used for analysis of discrete modes (Tollmien-Schlichting-like modes) only.[4] After clarification of uncertainties associated with the continuous spectra,[1] the method was also applied to the analysis of roughness-induced perturbations.[5–8] In order to find the amplitude of a normal mode, one needs profiles of the velocity, temperature, and pressure perturbations, together with some of their streamwise derivatives, given at only one station downstream from the disturbance source. Because computational results can provide all the necessary information about the perturbation field, the application of the multimode decomposition is straightforward. However, the first application of multimode decomposition was carried out for analysis of experimental data in a laminar wall jet when only one velocity component was measured.[9] The main feature of the laminar wall jet is that two unstable modes can coexist in the flow. This allowed the assumption that these modes provide the main input into the measured signal somewhere far downstream from an actuator. Therefore, the decomposition became possible with the help of one velocity component measured at a downstream station. Comparisons of recovered and measured data illustrated good agreement.

The objective of the present work is to demonstrate how the multimode decomposition may serve as a tool for gaining insight into the computational results and validating them as well. As an example, the direct numerical simulations (DNS) of high-speed boundary layer receptivity to wall blowing-suction are chosen for the analysis.[10] The perturbation flow field obtained in the DNS is projected onto the spatially growing/decaying modes of discrete and continuous spectra at a prescribed frequency. In addition, the filtered-out amplitudes of two discrete normal modes and of the fast acoustic modes are compared with ones predicted by the linear receptivity theory.

Briefly, the structure of the paper is as follows. Setup of the direct numerical simulation and the results used in the multimode decomposition are presented in Sec. II. A brief

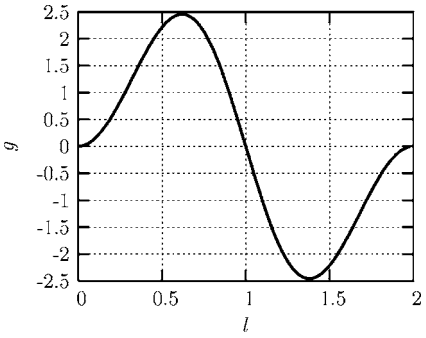

FIG. 1. Amplitude distribution of the blowing-suction slot.

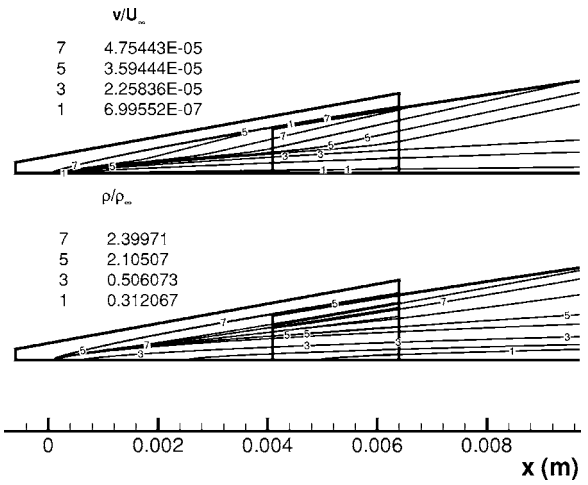

FIG. 2. Wall-normal velocity and density contours near the leading edge of the steady base flow obtained by a combination of a fifth-order shock-fitting method and a second-order TVD scheme.

description of the theoretical approach is provided in Sec. III. Decompositions of the computational results and their comparisons with the theoretical prediction are described in Sec. IV. In Sec. V, we discuss the results and outline their possible extensions.

II. NUMERICAL APPROACH

A numerical simulation was carried out by Wang and Zhong[10] to determine the receptivity of a Mach 8.0 flow over a sharp wedge to wall blowing-suction through a slot on the wedge surface. The wedge had a half-angle of 5.3°. The freestream parameters were as follows: velocity $U_\infty=1181.7$ m/s, density $\rho_\infty=0.0247\text{kg/m}^3$, and temperature $T_\infty=54.78$ K. Such a hypersonic boundary-layer flow had been numerically studied by other researchers. Malik *et al.*[11] solved the linearized Navier-Stokes equations to investigate the responses of the flow to three types of external forcing. Ma and Zhong[12] studied receptivity mechanisms of the same flow to various freestream disturbances by solving the two-dimensional compressible Navier-Stokes equations. In the current simulation, we extend the study to the receptivity mechanism of the hypersonic boundary layer to wall blowing-suction disturbances.

In our simulation, the Mach 8 flow is assumed to be thermally and calorically perfect. The governing equations for the simulation are the two-dimensional Navier-Stokes equations in the conservative form, i.e.,

$$\frac{\partial \mathbf{U}}{\partial t}+\frac{\partial}{\partial x_1}(\mathbf{F}_{1i}+\mathbf{F}_{1v})+\frac{\partial}{\partial x_2}(\mathbf{F}_{2i}+\mathbf{F}_{2v})=0, \tag{1}$$

where $\mathbf{U}$ is a vector containing the conservative variables of mass, momentum, and energy, i.e.,

$$\mathbf{U}=\{\rho,\rho u_1,\rho u_2,e\}. \tag{2}$$

The flux vector in (1) is divided into its inviscid and viscous components, because the two components are discretized with two finite-difference schemes: $\mathbf{F}_{1i}$ and $\mathbf{F}_{2i}$ are inviscid flux vectors, whereas $\mathbf{F}_{1v}$ and $\mathbf{F}_{2v}$ are viscous flux vectors. The flux vectors can be expressed as

$$\mathbf{F}_{ji}=\begin{bmatrix}\rho u_j\\ \rho u_1u_j+p\delta_{1j}\\ \rho u_2u_j+p\delta_{2j}\\ u_j(e+p)\end{bmatrix}, \tag{3}$$

$$\mathbf{F}_{jv}=\begin{bmatrix}0\\ -\tau_{1j}\\ -\tau_{2j}\\ -\tau_{nj}u_n-\kappa\dfrac{\partial T}{\partial x_j}\end{bmatrix}, \tag{4}$$

with $j,n\in\{1,2\}$. In the perfect gas assumption, pressure and energy are given by

$$p=\rho RT, \tag{5}$$

$$e=\rho c_vT+\frac{\rho}{2}(u_1^2+u_2^2), \tag{6}$$

where c_v is the specific heat at constant volume. For compressible Newtonian flow, the viscous stress tensor can be written as

$$\tau_{ij}=\mu\left(\frac{\partial u_i}{\partial x_j}+\frac{\partial u_j}{\partial x_i}\right)-\frac{2}{3}\mu\frac{\partial u_n}{\partial x_n}\delta_{ij}, \tag{7}$$

for $i,j,n\in\{1,2\}$. In the simulation, the viscosity coefficient, μ, and the heat conductivity coefficient, κ, are calculated using Sutherland's law together with a constant Prandtl number, Pr=0.72.

The fifth-order shock-fitting method of Zhong[13] is used to solve the two-dimensional Navier-Stokes equations in a domain bounded by the bow shock and the wedge surface. The bow shock is treated as a boundary of the computational domain, which makes it possible for the Navier-Stokes equations to be spatially discretized by high-order finite-difference methods. Specifically, a fifth-order upwind scheme is used to discretize the inviscid flux derivatives. Meanwhile, the viscous flux derivatives are discretized by a

sixth-order central scheme. The Rankine-Hugoniot relation across the shock and a characteristic compatibility relation from the downstream flow field are combined to solve the flow variables behind the shock. By using the shock-fitting method, the interaction between the unsteady perturbations and the bow shock is solved as part of the solutions, with the position and velocity of the shock front being taken as unknown flow variables. A three-stage semi-implicit Runge-Kutta method is used for temporal integration, where the time step size is obtained based on the CFL number and grid size.

The steady base flow is computed by solving (1) with a combination of the fifth-order shock-fitting method and a second-order TVD scheme. In the leading edge region, there exists a singular point at the tip of the wedge, which will introduce numerical instability if the fifth-order shock-fitting method is used to simulate the flow. Therefore, the computational domain for the shock-fitting simulation starts from a very short distance downstream of the leading edge. A second-order TVD scheme is used to simulate the steady base flow in a small region including the leading edge to supply inlet conditions for the shock-fitting simulation. The steady base flow simulation is advanced in time until the last pair of solutions separated by a finite time interval can be considered as identical within a specified tolerance. For unsteady simulations, blowing-suction disturbances are introduced in a downstream region where the shock-fitting method is used. The subsequent responses of the hypersonic boundary layer are simulated with the fifth-order shock-fitting method to achieve a periodic-in-time flow field (large time asymptote of perturbation calculations).

For the simulation of steady base flow, the wall is adiabatic, and the physical boundary condition of velocity on the wedge surface is the nonslip condition. When periodic-in-time blowing-suction disturbances are enforced on the steady base flow, the isothermal temperature condition is applied on the wall. This temperature condition is a standard boundary condition for theoretical and numerical studies of high-frequency disturbances. Meanwhile, a nonslip condition is applied on the wall, except for the forcing region. Inlet conditions are specified, while high-order extrapolation is used for outlet conditions because the flow is supersonic at the exit boundary, except for a small region near the wedge surface.

In the current study, the coordinate x is defined as the distance measured from the tip of the wedge, whereas the coordinate y is the normal distance from the wall. The blowing-suction slot is simulated by the periodic-in-time boundary conditions for the perturbation of the mass flux on the wall, which can be written as follows:

$$\rho v = q_0 g(l) \sum_{n=1}^{15} \sin(\omega_n t), \tag{8}$$

where q_0 is an amplitude parameter and ω_n is the circular frequency of multifrequency perturbations. In (8), $g(l)$ is the profile function defined as

$$g(l) \begin{cases} 20.25l^5 - 35.4375l^4 + 15.1875l^2, & (l \leqslant 1); \\ -20.25(2-l)^5 + 35.4375(2-l)^4 - 15.1875(2-l)^2, & (l > 1). \end{cases} \tag{9}$$

The variable l in (9) is a nondimensional coordinate defined within the blowing-suction slot,

$$l(x) = \frac{2(x - x_i)}{(x_e - x_i)}, \quad x_i \leqslant x \leqslant x_e, \tag{10}$$

where x_i and x_e are the coordinates of the leading and the trailing edges of the slot, respectively. The amplitude distribution, $g(l)$, is shown in Fig. 1. Numerical simulations reveal that there is no difference in the results if surface blowing suction is specified by the perturbation in the y velocity only. This is due to the fact that the weak perturbation is in the linear region. The corresponding velocity perturbation at $y = 0$ is

$$v(x,t) = v_w(x) \sum_{n=1}^{15} \sin(\omega_n t) = \frac{q_0}{\rho_{sw}} g(l) \sum_{n=1}^{15} \sin(\omega_n t), \tag{11}$$

where ρ_{sw} is density of the unperturbed flow on the wall. In the theoretical analysis presented in Sec. III, we utilize (11) as the boundary condition simulating the actuation.

As was mentioned above, the steady base flow is simulated with a combination of a fifth-order shock-fitting finite-difference method and a second-order TVD scheme. In the leading edge region, there exists a singular point at the tip of the wedge, which will introduce numerical instability if the fifth-order shock-fitting method is used to simulate the flow. Therefore, the computational domain for the fifth-order shock-fitting method starts at $x = 0.00409$ m and ends at $x = 1.48784$ m. In actual simulations, the computational domain is divided into 30 zones, with a total of 5936 grid points in the streamwise direction and 121 grid points in the wall-normal direction. Forty-one points are used in the buffering region between two neighboring zones, which proved to be sufficient to make the solution accurate and smooth within the whole domain. An exponential stretching function is used in the wall-normal direction to cluster more points inside the boundary layer. On the other hand, the grid points are uniformly distributed in the streamwise direction.

For the first zone of the shock-fitting calculations, the inlet conditions are obtained from the results of the second-order TVD shock-capturing scheme, which is used to simu-

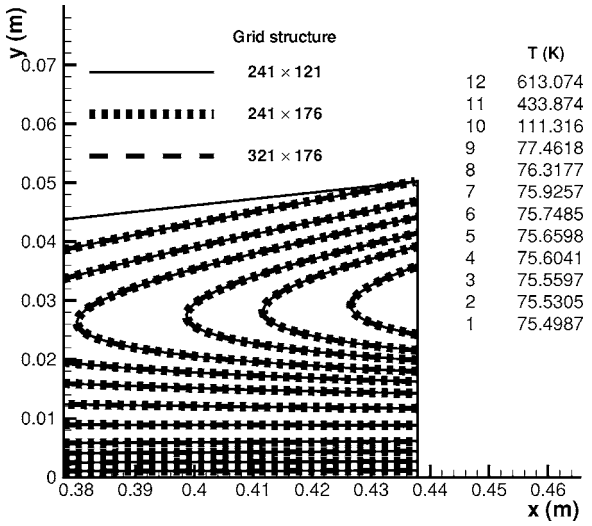

FIG. 3. Comparison of temperature contours of the steady base flow in zone 10 simulated using the three sets of grids.

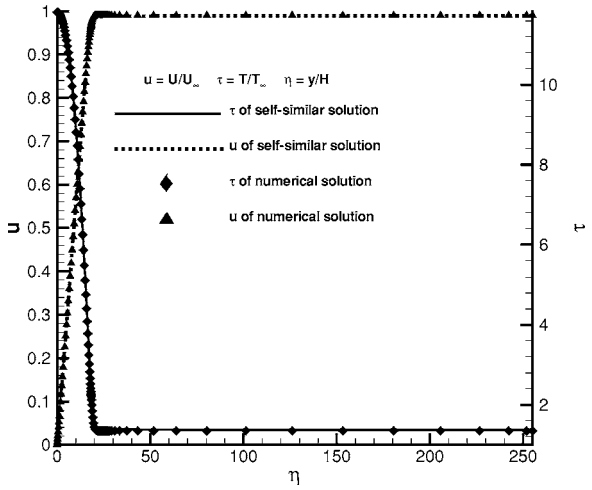

FIG. 4. Profiles of streamwise velocity and temperature in the wall-normal direction at the location of $x=0.62784$ m.

late the steady base flow in a small region including the leading edge. For other zones, inlet conditions are interpolated from the results of the previous zone. Figure 2 shows the wall-normal velocity and density contours near the leading edge of the steady base flow obtained by the second-order TVD scheme and the fifth-order shock-fitting method. The flow field including the leading edge is simulated by the TVD scheme, while the flow field after $x=0.00409$ m is simulated by the shock-fitting method. It shows that wall-normal velocity and density contours have good agreement within the buffering region, which indicates that the TVD solutions are accurate for use as inlet conditions for the fifth-order shock-fitting simulation in the first zone.

In our simulations, three sets of grid structures are tested to check the grid independence of the numerical results. As an example, Fig. 3 compares the temperature contours of the steady base flow in zone 10, simulated using the three sets of grids. It shows that the three contours agree well in the domain despite the increases in grid points. This figure indicates that the simulation results are converged in both the x and y directions. Figure 4 shows the streamwise velocity and temperature profiles in the wall-normal direction at the location of $x=0.62784$ m. The current numerical solutions are compared with the self-similar boundary-layer solutions. In the figure, velocity and temperature are nondimensionalized by corresponding freestream values, while the y coordinate is nondimensionalized by $\sqrt{x\mu_\infty/\rho_\infty U_\infty}$. This figure shows that the properties of the current numerical simulation agree very well with those of the self-similar boundary-layer solution. In unsteady simulations, the amplitude of blowing-suction is at least one order of magnitude larger than the maximum numerical noise and it is small enough to preserve the linear properties of the disturbances. Figure 5 compares the dimensionless amplitude along the wedge surface of a pressure perturbation at a frequency of 149.2 kHz. The solid line and triangular symbol represent the numerical results simulated using grid structures of 241×176 and 241×121, respectively. The agreement between the two distributions of perturbation amplitude indicates that the grid independence of unsteady simulation is achieved. All these three figures show that the grid structure of 241×121 used in the current simulation is enough to ensure grid-independent numerical simulations.

For the purpose of the multimode decomposition, the fast Fourier transform (FFT) of the perturbation field is carried out downstream from the slot at distance x_{data}. The time duration of simulation data used for FFT analysis is one period of the base frequency. Seven cases with different x_i, x_e, and x_{data} are considered in the present work. In all cases, the width of the slot, $w=x_e-x_i$, is kept equal to 1.2 cm. Coordinates of the slot center, x_c, and the coordinates x_{data} are presented in Table I.

Figure 6 shows an example of the streamwise velocity amplitude distributions obtained in the numerical simulation for case 1. The velocity is scaled with the edge velocity, $U_e=1167.3$ m/s, and the distance from the wall is scaled with $H=0.1251$ mm. The length scale H is defined as

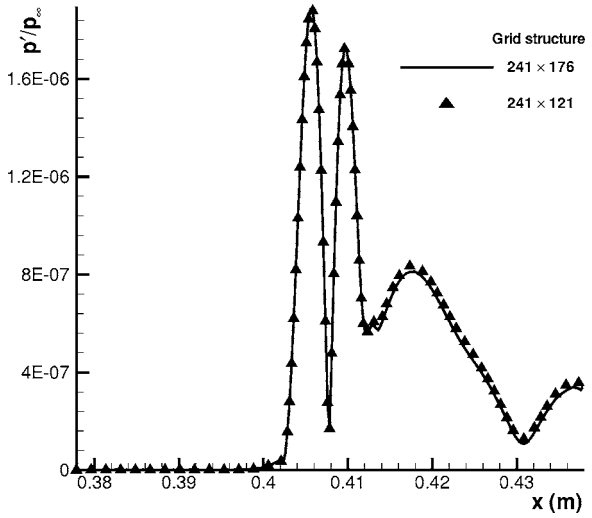

FIG. 5. Comparison of dimensionless amplitude along the wedge surface of pressure perturbation at the frequency of 149.2 kHz.

TABLE I. Coordinates of the slot center, x_c; the coordinate of the station, x_{data}, where data were provided for the decomposition; the amplitude parameter q_0 in (8); the length scales corresponding to the considered examples; the local boundary layer thickness, δ_{99}; and the real and imaginary parts of the eigenvalues corresponding to the slow and fast discrete modes, α_S and α_F, respectively. The presented eigenvalues correspond to frequencies $(N-1)\times 14.92$ kHz, where N is given in the table.

Case	x_c (m)	x_{data} (m)	$q_0\times 10^5$ (kg/s m^2)	H (mm)	δ_{99} (mm)	N	$\alpha_{Sr}H$ / $\alpha_{Si}H$	$\alpha_{Fr}H$ / $\alpha_{Fi}H$
1	0.10772	0.12784	0.125188	0.1251	2.437	11	$+1.07\times10^{-1}$	$+9.91\times10^{-2}$
							-3.38×10^{-4}	$+2.73\times10^{-3}$
2	0.40784	0.42784	0.054453	0.2289	4.452	7	$+1.17\times10^{-1}$	$+1.15\times10^{-1}$
							-1.98×10^{-3}	$+6.92\times10^{-3}$
3	0.05784	0.07784	0.214139	0.09764	1.901	11	$+8.54\times10^{-2}$	$+7.19\times10^{-2}$
							$+5.77\times10^{-6}$	$+8.16\times10^{-4}$
4	0.15784	0.17784	0.096130	0.1476	2.875	10	$+1.13\times10^{-1}$	$+1.09\times10^{-1}$
							-1.14×10^{-3}	$+6.75\times10^{-3}$
5	0.20784	0.22784	0.080666	0.1670	3.250	9	$+1.14\times10^{-1}$	$+1.10\times10^{-1}$
							-1.28×10^{-3}	$+6.63\times10^{-3}$
6	0.25784	0.27784	0.070759	0.1845	3.590	8	$+1.10\times10^{-1}$	$+1.05\times10^{-1}$
							-6.05×10^{-4}	$+6.89\times10^{-3}$
7	0.30784	0.32784	0.063745	0.2004	3.900	8	$+1.19\times10^{-1}$	$+1.19\times10^{-1}$
							-2.43×10^{-3}	$+7.55\times10^{-3}$

$\sqrt{x_{\text{data}}\mu_\infty/\rho_\infty U_\infty}$. The boundary layer thickness δ_{99} (distance from the wall where the local velocity $U=0.99U_e$) is given in Table I. As follows from the table, the ratio δ_{99}/H is about 19.5 in all cases.

The contours of the instantaneous pressure perturbation induced by blowing-suction disturbance at frequency 5×14.92 kHz are shown in Fig. 7 (case 2). After the blowing-suction slot, the excited pressure perturbations are divided into two branches: one branch penetrates the boundary layer and propagates along the Mach lines (acoustic waves) while the other branch stays within the boundary layer, which is the instability mode (mode S in the terminology of Sec. IV), indicated by the typical wave structures near the wall.

III. THEORETICAL ANALYSIS

The theoretical analysis of the numerical results in the present work includes two steps. The first one is the decomposition of the perturbation field obtained in the computational part of the work into normal modes (projection onto the basis comprised of the eigenfunctions of the continuous and discrete spectra). The second step is the receptivity problem solution with the blowing suction on the wall defined by (11) and comparison of the found amplitudes with those filtered out from the computational results.

The multimode decomposition of two-dimensional perturbations in compressible boundary layers was introduced by Gaydos and Tumin[2] (GT), and it can be utilized for analysis of the present problem. Alternatively, one can use the results for three-dimensional perturbations[3] when the spanwise wave number, β, is very small. Similarly, the receptivity problem solution for three-dimensional perturbations introduced on the wall[7] can be utilized for analysis of the two-dimensional problem by using $\beta\to 0$. For clarity of the

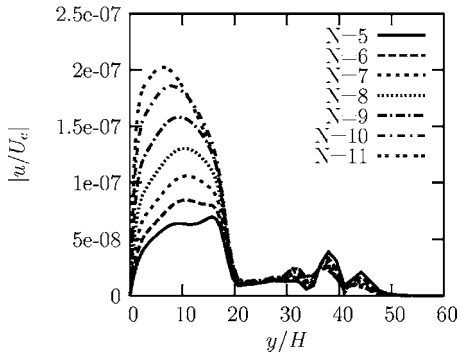

FIG. 6. Amplitude distribution of the streamwise velocity component at $x=x_{\text{data}}$ and frequency $(N-1)\times 14.92$ kHz for case 1.

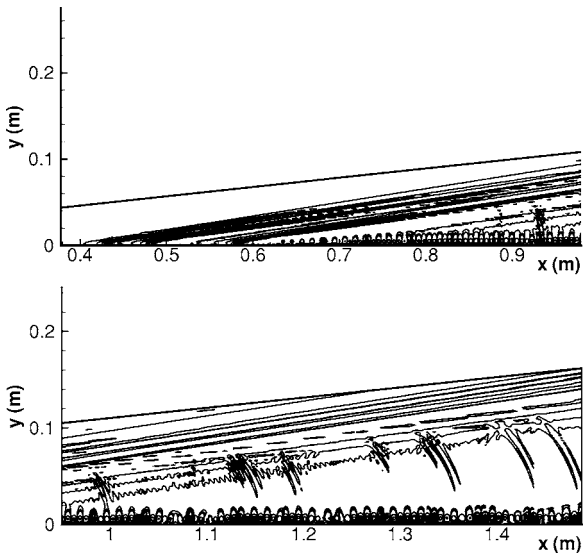

FIG. 7. Contours of the instantaneous pressure perturbation induced by blowing-suction disturbance at frequency 5×14.92 kHz for case 2.

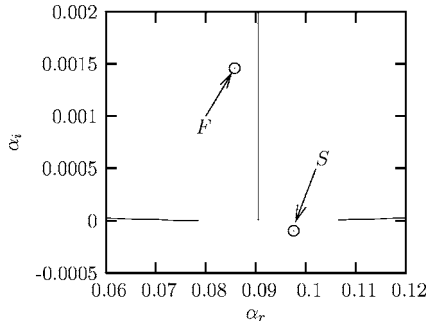

FIG. 8. Continuous and discrete spectra at 134.28 kHz for case 1.

method description, we recapitulate the receptivity problem solution in a form adequate for two-dimensional perturbations in a compressible boundary layer.[14] One can find a historical perspective of the method and relevant bibliography in Refs. 7 and 8.

In the parallel flow approximation, we write down the governing equations for a two-dimensional periodic-in-time perturbation in the matrix notation of GT,

$$\frac{\partial}{\partial y}\left(\mathbf{L}_0\frac{\partial \mathbf{A}}{\partial y}\right)+\mathbf{L}_1\frac{\partial \mathbf{A}}{\partial y}=\mathbf{H}_1\mathbf{A}+\mathbf{H}_2\frac{\partial \mathbf{A}}{\partial x}, \tag{12}$$

where $\mathbf{L}_0$, $\mathbf{L}_1$, $\mathbf{H}_1$, and $\mathbf{H}_2$ are 9×9 matrices. Their nonzero elements are given in GT. Vector $\mathbf{A}$ is comprised of the perturbation profiles and their derivatives,

$$\mathbf{A}=(u,\partial u/\partial y,v,\pi,\theta,\partial\theta/\partial y,\partial u/\partial x,\partial v/\partial x,\partial\theta/\partial x)^T, \tag{13}$$

where u and v are x- and y-velocity components, respectively; π is the pressure perturbation; θ is the temperature perturbation; and T stands for transposed. In the case of blowing suction through a slot, the boundary conditions in the slot domain are inhomogeneous, $A_3(x,0)=v_w(x)$, and A_8 can be found from A_3 by the definition. The solution of (12) is decaying outside the boundary layer. For simplicity, we assume that the perturbation frequency is subcritical, and one can employ the Fourier transform with respect to x,

$$\mathbf{A}_v(\alpha_v,y)=\int_{-\infty}^{+\infty}\mathbf{A}(x,y)e^{-i\alpha_v x}dx. \tag{14}$$

In the case of a supercritical frequency, one has to refer to Briggs' method in order to include the unstable mode (exponentially growing downstream mode) in the inverse Fourier transform.[15,16]

Vector function $\mathbf{A}_v(\alpha_v,y)$ satisfies the following equation and boundary conditions:

$$\frac{d}{dy}\left(\mathbf{L}_0\frac{d\mathbf{A}_v}{dy}\right)+\mathbf{L}_1\frac{d\mathbf{A}_v}{dy}=\mathbf{H}_1\mathbf{A}_v+i\alpha_v\mathbf{H}_2\mathbf{A}_v, \tag{15}$$

$$y=0:\quad A_{v1}=0,\quad A_{v3}=\varphi(\alpha_v),\quad A_{v5}=0, \tag{16a}$$

$$y\to\infty:\quad |A_{vj}|\to 0,\quad (j=1,\ldots,9), \tag{16b}$$

where

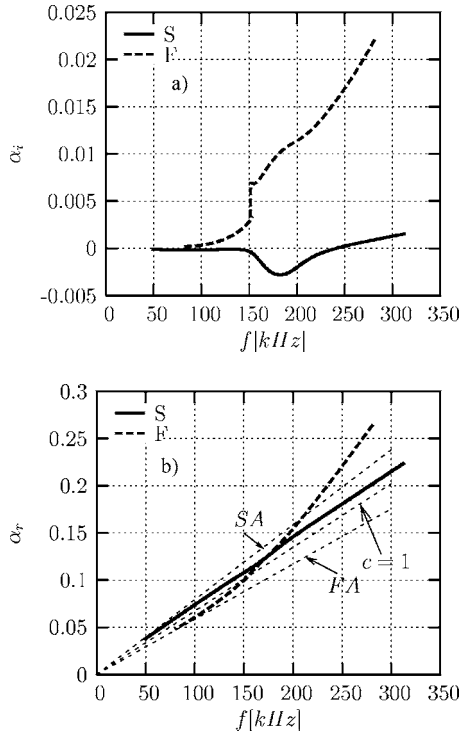

FIG. 9. Imaginary (a) and real (b) parts of the wave number, case 1.

$$\varphi(\alpha_v)=\int_{-\infty}^{+\infty}v_w(x)e^{-i\alpha_v x}dx. \tag{17}$$

.

Equation (15) has three fundamental solutions decaying outside the boundary layer. One can write down the solution of the inhomogeneous boundary-value problem as follows:

$$\mathbf{A}_v=C_1\mathbf{Z}_1+C_3\mathbf{Z}_3+C_5\mathbf{Z}_5, \tag{18}$$

where $\mathbf{Z}_1$, $\mathbf{Z}_3$, and $\mathbf{Z}_5$ are the decaying fundamental solutions. The coefficients C_j in (18) are found from the boundary conditions (16a) on the wall. The formal solution of (12) satisfying the boundary conditions can be written as follows:

$$\mathbf{A}(x,y)=\frac{1}{2\pi}\int_{-\infty}^{+\infty}\mathbf{A}_v(\alpha_v,y)e^{i\alpha_v x}d\alpha_v. \tag{19}$$

It was shown in Refs. 17 and 3 that the periodic-in-time solution of the linearized Navier-Stokes equations can be expanded into the normal modes of continuous and discrete spectra,

$$\mathbf{A}(x,y)=\sum_j\int_0^\infty C_j(k)\mathbf{A}_\alpha(y,k)e^{i\alpha_j(k)x}dk + \sum_m C_m\mathbf{A}_{\alpha_m}(y)e^{i\alpha_m x}, \tag{20}$$

where the eigenfunctions $\mathbf{A}_\alpha$ are found as solutions of the following problem:

$$\frac{d}{dy}\left(\mathbf{L}_0\frac{d\mathbf{A}_\alpha}{dy}\right)+\mathbf{L}_1\frac{d\mathbf{A}_\alpha}{dy}=\mathbf{H}_1\mathbf{A}_\alpha+i\alpha\mathbf{H}_2\mathbf{A}_\alpha, \tag{21}$$

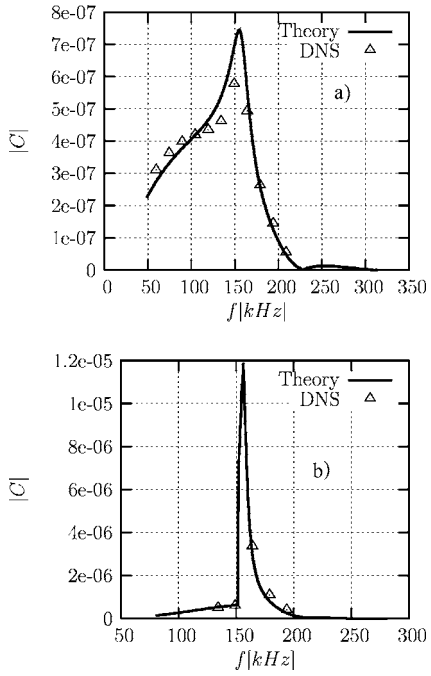

FIG. 10. Comparison of the theoretical prediction for the receptivity coefficient in case 1 with data filtered out from the computational results: (a) mode S and (b) mode F.

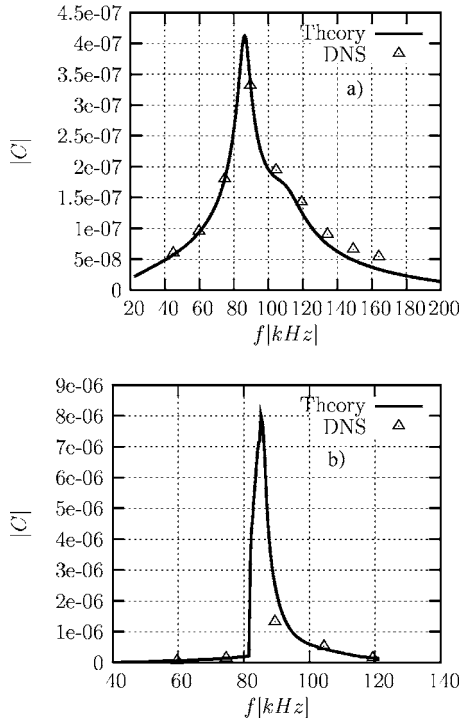

FIG. 11. Comparison of the theoretical prediction for the receptivity coefficient in case 2 with data filtered out from the computational results: (a) mode S and (b) mode F.

$$y=0: \quad A_{\alpha 1}=A_{\alpha 3}=A_{\alpha 5}=0, \tag{22a}$$

$$y\to\infty: \quad |A_{\alpha j}|<\infty, \quad (j=1,\ldots,9). \tag{22b}$$

.

The first term in (20) represents summation over the modes of the continuous spectrum (such as entropy, vorticity, and acoustic modes), and the second term represents input of the discrete modes. Eigenfunctions of the discrete modes decay outside the boundary layer, whereas eigenfunctions of the continuous spectra have asymptotic behavior $\sim\exp(\pm iky)$ at $y\to\infty$, where k is a real parameter $(k>0)$. This parameter also serves as a coordinate along the branches of the continuous spectra in (20).

Vectors $\mathbf{A}_\alpha$ together with the solution of the adjoint problem, $\mathbf{B}_\alpha$,

$$\frac{d}{dy}\left(\mathbf{L}_0^T\frac{d\mathbf{B}_\alpha}{dy}\right)-\mathbf{L}_1^T\frac{d\mathbf{B}_\alpha}{dy}=\mathbf{H}_1^T\mathbf{B}_\alpha+i\alpha\mathbf{H}_2^T\mathbf{B}_\alpha, \tag{23}$$

$$y=0: \quad B_{\alpha 2}=B_{\alpha 4}=B_{\alpha 6}=0, \tag{24a}$$

$$y\to\infty: \quad |B_{\alpha j}|<\infty, \quad (j=1,\ldots,9), \tag{24b}$$

represent the biorthogonal eigenfunction system $\{\mathbf{A}_\alpha,\mathbf{B}_\alpha\}$. There is the following orthogonality relation:

$$\langle\mathbf{H}_2\mathbf{A}_\alpha,\mathbf{B}_{\alpha'}\rangle\equiv\sum_{j=1}^{9}\int_0^\infty(\mathbf{H}_2\mathbf{A}_\alpha)_jB_{\alpha' j}dy=Q\Delta_{\alpha,\alpha'}, \tag{25}$$

where $\Delta_{\alpha,\alpha'}$ is the Kronecker delta if α or α' belongs to the discrete spectrum, and $\Delta_{\alpha,\alpha'}=\delta(\alpha-\alpha')$ is the delta function if both α and α' belong to the continuous spectrum. The coefficient Q on the right-hand side of (25) depends on the normalization of $\mathbf{A}_\alpha(y)$ and $\mathbf{B}_\alpha(y)$. Evaluation of the coefficient in the case of the discrete spectrum is straightforward. In the case of the continuous spectrum, the coefficient can be found with the help of the fundamental solutions outside the boundary layer.[1,3]

The orthogonality relation (25) provides a tool to find coefficients C_j and C_m in the formal solution (19). With the help of the orthogonality relation (25), one can find the initial amplitude of a mode entering in the formal solution $\mathbf{A}(x,y)$,

$$C=\frac{\langle\mathbf{H}_2\mathbf{A}(x,y),\mathbf{B}_\alpha(y)\rangle}{Q}e^{-i\alpha x}. \tag{26}$$

.

If we consider a dot product of $\mathbf{B}_\alpha$ and (15), and integrate with respect to y over the interval $[0,\infty)$, we arrive at the following identity (we take into account explicit forms of matrices $\mathbf{L}_0$ and $\mathbf{L}_1$):

$$\left[L_0^{43}A_{v3}\frac{dB_{\alpha 4}}{dy}-A_{v3}B_{\alpha 3}\right]_{y=0}+\left\langle\mathbf{A}_v,\frac{d}{dy}\left(\mathbf{L}_0^T\frac{d\mathbf{B}_\alpha}{dy}\right)\right\rangle-\left\langle\mathbf{A}_v,\mathbf{L}_1^T\frac{d\mathbf{B}_\alpha}{dy}\right\rangle=\langle\mathbf{A}_v,\mathbf{H}_1^T\mathbf{B}_\alpha\rangle+i\alpha_v\langle\mathbf{A}_v,\mathbf{H}_2^T\mathbf{B}_\alpha\rangle, \tag{27}$$

where L_0^{43} stands for the element of matrix $\mathbf{L}_0$ having indices (4,3). Taking into account the adjoint equation (23), one can substitute the formal solution (19) in (26) and find, with the help of (27), the following result:

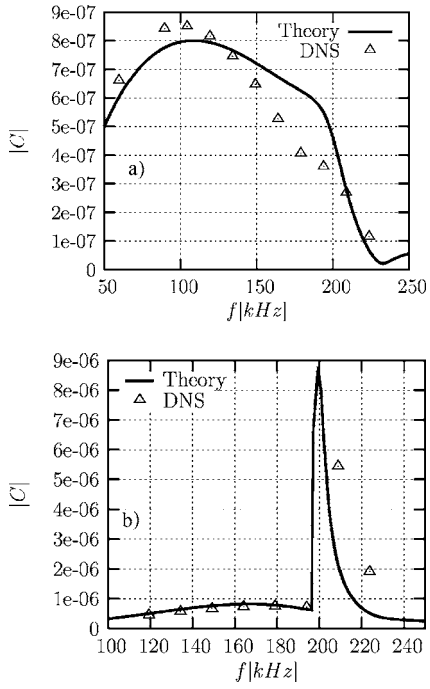

FIG. 12. Comparison of the theoretical prediction for the receptivity coefficient in case 3 with data filtered out from the computational results: (a) mode S and (b) mode F.

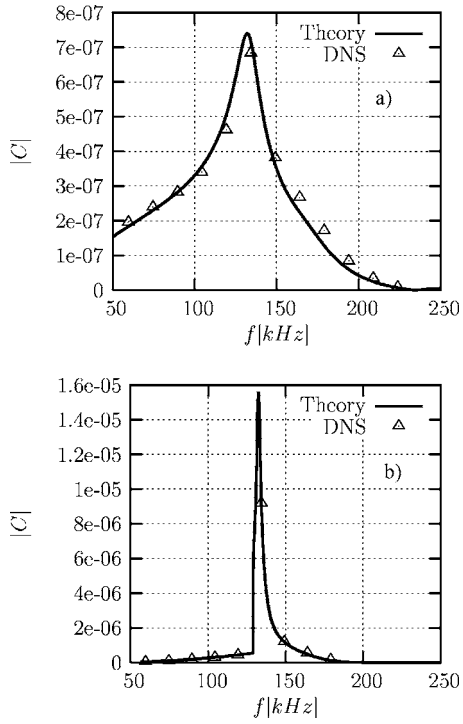

FIG. 13. Comparison of the theoretical prediction for the receptivity coefficient in case 4 with data filtered out from the computational results: (a) mode S and (b) mode F.

$$C = \frac{1}{2\pi}\frac{1}{Q}\int_{-\infty}^{+\infty} e^{i(\alpha_v-\alpha)x}\varphi(\alpha_v)\frac{\left[L_0^{43}\dfrac{dB_{\alpha 4}}{dy} - B_{\alpha 3}\right]_{y=0}}{i(\alpha_v-\alpha)}d\alpha_v. \tag{28}$$

By closing the path of the integral in the upper half-plane, we find the theoretical coefficient as the residue value at the pole $\alpha_v=\alpha$,

$$C = \frac{\varphi(\alpha)}{Q(\alpha)}\left[L_0^{43}\frac{dB_{\alpha 4}}{dy} - B_{\alpha 3}\right]_{y=0}. \tag{29}$$

On the other hand, we have results of the direct numerical simulation (DNS) in the form of the vector function $\mathbf{A}_{\mathrm{DNS}}$ at $x=x_{\mathrm{DNS}}$. One can find from (26) the initial amplitude, C_{DNS}, of the mode as follows:

$$C_{\mathrm{DNS}} = \frac{\langle \mathbf{H}_2\mathbf{A}_{\mathrm{DNS}}(x_{\mathrm{DNS}},y),\mathbf{B}_\alpha\rangle}{Q(\alpha)}e^{-i\alpha x_{\mathrm{DNS}}}. \tag{30}$$

According to the definition of coefficients in (20), C in (29) and C_{DNS} in (30) are the complex amplitudes at $x=0$. In order to interpret the complex weight C in (29) as initial amplitude and phase of the normal mode generated by the slot, the origin, $x=0$, is chosen at the slot center. Therefore, x_{DNS} in (30) means the distance $x_{\mathrm{data}}-x_c$, where x_{data} and x_c are given in Table I for each case. Because the distance x_{DNS} in all considered examples is less than $11\delta_{99}$, the nonparallel effects in the growing/decaying of the perturbations on the interval x_{DNS} are ignored. If one is interested in the local amplitude of a mode at $x=x_{\mathrm{DNS}}$, the origin of the coordinate should be at this point. In other words, $x_{\mathrm{DNS}}=0$ in (30).

Finally, one can compare the filtered-out coefficient C_{DNS} in (30) with the predicted C in (29).

IV. RESULTS

A. Discrete modes

One can find the details of the numerical method used for computation of the eigenvalues and eigenfunctions of the direct and adjoint problems elsewhere.[3] In all cases, eigenvalues and eigenfunctions of the discrete and continuous spectra are computed using the velocity, temperature, and viscosity profiles obtained from the direct numerical simulation at $x=x_{\mathrm{data}}$.

Figure 8 shows the discrete and continuous spectra at frequency $f=134.28$ kHz. One can see in Fig. 8 slow (S) and fast (F) discrete modes, and branches of the continuous spectra. There are two horizontal branches representing the slow and fast acoustic modes. Their branching points correspond to phase velocities $c=1\mp 1/M$, where M is the local Mach number at the edge of the boundary layer. At this scale, the vertical branch is comprised of two indistinguishable branches of entropy and vorticity modes.[3]

Figure 9 shows the imaginary and real parts of the wave number α for the discrete modes as functions of frequency, ω. Lines SA and FA in Fig. 9(b) represent the branching points $(k=0)$ of the slow and fast acoustic modes, respectively. One discrete mode (mode F) is synchronized with the fast acoustic mode at low frequencies, whereas the other discrete mode (mode S) is synchronized with the slow acoustic mode.

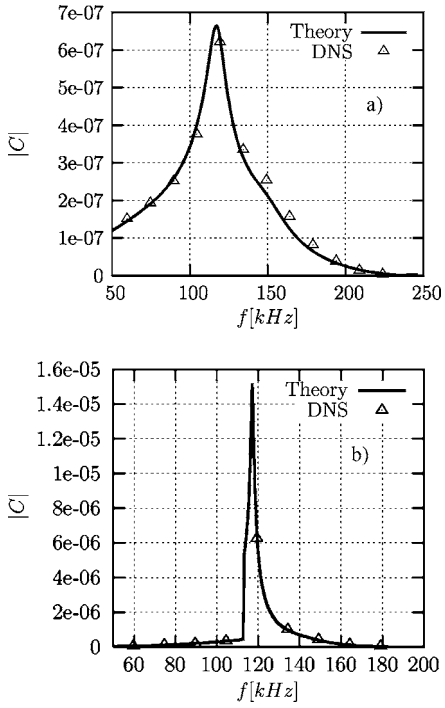

FIG. 14. Comparison of the theoretical prediction for the receptivity coefficient in case 5 with data filtered out from the computational results: (a) mode S and (b) mode F.

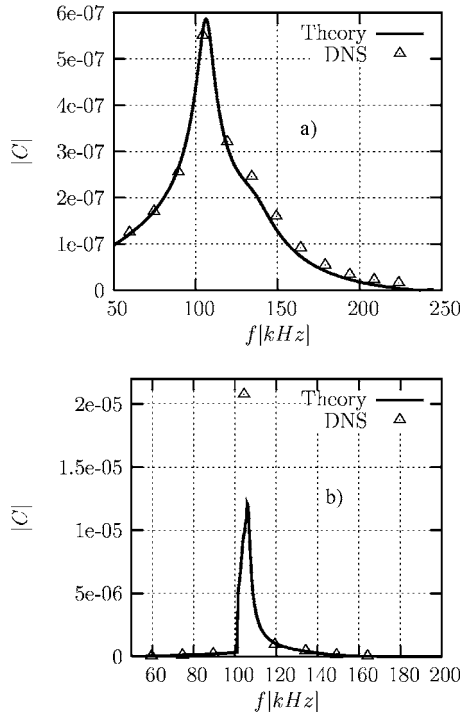

FIG. 15. Comparison of the theoretical prediction for the receptivity coefficient in case 6 with data filtered out from the computational results: (a) mode S and (b) mode F.

At $f \approx 150$ kHz, mode F is synchronized with the vorticity and entropy modes ($c=1$). This synchronization is accompanied by a discontinuity in α_i. The phenomenon may be illustrated as a sequence of Fig. 8 at different frequencies. When frequency increases, the vertical branch in Fig. 8 is moving from left to right with speed $d\alpha_r/d\omega=1$, whereas the eigenvalue corresponding to the fast discrete mode moves from left to right with $d\alpha_r/d\omega>1$. At some frequency, the discrete mode coalesces with the branch of the continuous spectrum. As was discussed in Ref. 18, the discrete mode coalesces with the continuous spectrum from one side of the branch cut and reappears on the other side at another point. Mathematically, the eigenvalue associated with mode F approaches one side of the branch cut on the complex α plane. As the pole on the plane coalesces with the branch cut, it moves to the upper Riemann sheet while, simultaneously, the pole that was on the lower Riemann sheet moves into the complex α plane at another point. Actually, one should interpret these poles as two different modes. Historically, they are discussed as one mode having the discontinuity.

At higher frequency, $f \approx 170$ kHz, there is a synchronism between mode F and mode S. However, there is no coalescence of the eigenvalues. A model of two-mode synchronism considered by Fedorov and Khokhlov[19,20] explained the branching of the modes at the point of synchronism. At this point, one of the modes becomes unstable, whereas the other one moves toward positive α_i. Although in this example the modes have the same phase velocity $c=\omega/\alpha_r$ at $f \approx 170$ kHz, the minimum of $|\alpha_F-\alpha_S|$ exists in the vicinity of $f \approx 150$ kHz, and, actually, this is the point where we observe the modes' branching.

Both the slow and fast discrete modes could be involved in the laminar-turbulent transition scenario. For example, the decaying mode could be generated by the entropy or vorticity modes of the continuous spectra. At the point of synchronism between the fast and slow modes, the decaying mode can give rise to the unstable mode (switching of the modes), which may lead to the transition. The scenario suggested by Fedorov and Khokhlov[20] means that both the stable and unstable modes are of interest for understanding transition mechanisms. Later on, switching of the modes was observed in direct numerical simulations of perturbations in high-speed boundary layers.[21] These features of the fast and slow discrete modes explain why we need accurate simulations of the decaying mode as well.

Figure 10 shows a comparison of the theoretical receptivity coefficient with the amplitude filtered out from the computational results in accordance with (30). The results in Fig. 10 and what follows for the discrete modes correspond to normalization of the eigenfunctions when the maximum of the mass flux perturbation in the boundary layer is equal to 1. Figures 11–16 demonstrate comparisons of theoretical and numerical results for cases 2 through 7, respectively.

One can see from the figures that there is a good agreement between amplitudes calculated with the help of the receptivity model of III and those obtained from the numerical results as a projection onto the normal modes.

One can also notice that the shape of the function $|C(f)|$ for mode S in case 3 [Fig. 12(a)] is qualitatively different from the other cases, and agreement between the theoretical prediction and the numerical results is not as good. Case 3 corresponds to the closest location of the slot to the wedge's tip. The slot has a width of about 1.2 cm, whereas the dis-

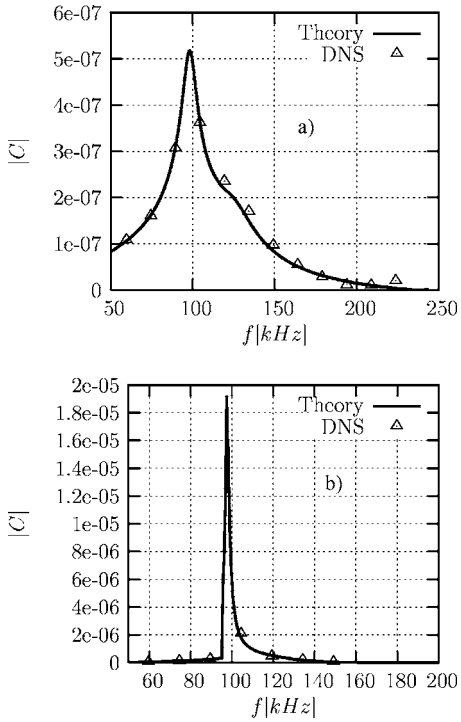

FIG. 16. Comparison of the theoretical prediction for the receptivity coefficient in case 7 with data filtered out from the computational results: (a) mode S and (b) mode F.

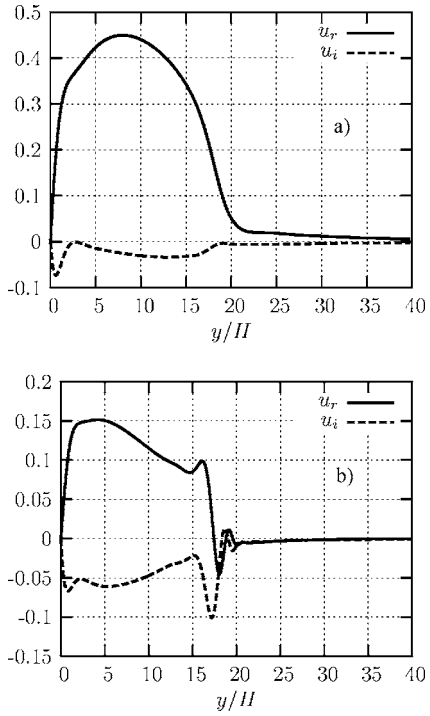

FIG. 17. Streamwise velocity perturbation in discrete mode F: (a) 89.52 kHz ($c=1.059$) and (b) 119.36 kHz ($c=0.926$).

tance from the tip is about 5 cm, and one should expect nonparallel flow effects, which were neglected in the present model. The nonparallel flow effects may be incorporated into the receptivity problem solution with the help of the multiple scales method along the lines of the distributed receptivity model proposed by Choudhari.[22] Another approach to receptivity problems with nonparallel flow effects was suggested by Bertolotti.[23] Because the main objective of the present work was decomposition of the DNS results, we do not pursue the nonparallel flow effects in the theoretical solution of the receptivity problem.

The most significant discrepancy between the theory and the computational results is observed for mode F in case 6 at $f=104.44$ kHz [Fig. 15(b)]. This example corresponds to the eigenvalue $\alpha=0.1047+i6.894\times10^{-3}$ located very close to the branch cut representing the vorticity/entropy modes having $\alpha_r\approx0.1036$. In order to illustrate the qualitative difference between the mode eigenfunctions when a mode is approaching the branch cut, we show in Fig. 17 streamwise velocity perturbations of the neighboring discrete modes at 89.52 and 119.36 kHz [phase velocities, c, of the modes in Figs.17(a) and 17(b) are equal to 1.059 and 0.926, respectively]. The streamwise velocity of mode F at $f=104.44$ kHz is shown in Fig. 18 ($c=0.99$). One can see that although the amplitude of the mode decays outside the boundary layer, as it has to for a discrete mode, there are oscillations in the amplitude distribution in y typical for modes of continuous spectra. The closer the location of the eigenvalue is to the branch cut, the more similarity with the continuous spectra should be observed.

Fedorov and Khokhlov[24] considered the receptivity problem when a synchronism between two discrete modes is possible. They showed that in this case $Q=\langle \mathbf{H}_2\mathbf{A}_\alpha,\mathbf{B}_\alpha\rangle\to0$, and the analysis has to include both modes simultaneously, together with the nonparallel flow effects. In our example, we have a synchronism between a discrete mode and the continuous spectrum. Figure 19 shows the magnitude $|Q|$ for modes F and S as functions of frequency. One can see that in the case of mode F, Q is very close to zero at $f=104.44$ kHz. This means that the theoretical model based on the parallel flow approximation is not adequate, and the extension of the model[24] to the case of a continuous spectrum is required.

B. Acoustic modes

The biorthogonal eigenfunction expansion also provides a tool for analysis of the input from continuous spectra in the computational results. Examples of boundary layers at

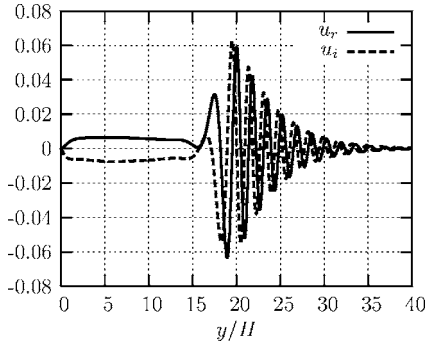

FIG. 18. Streamwise velocity perturbation in discrete mode F at $f=104.44$ kHz ($c=0.99$).

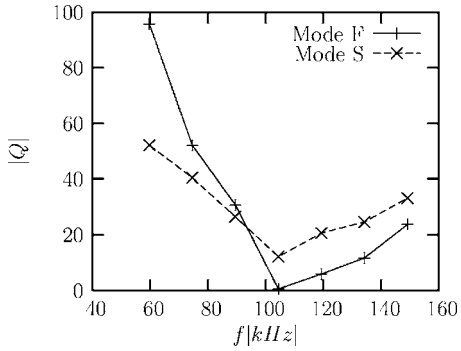

FIG. 19. Magnitude of the denominator in (30), case 6.

$M=2$ and 4.5 considered by Balakumar and Malik[16] and Tumin[7] indicate that input from entropy and vorticity modes due to blowing suction through the wall is small in comparison to the acoustic modes. Therefore, we are considering the fast and slow acoustic modes only (the horizontal branches in Fig. 8).

In the case of two-dimensional perturbations, eigenfunctions corresponding to the acoustic modes are comprised of four fundamental solutions.[2,17] Two of them decay exponentially outside the boundary layer, whereas the other two fundamental solutions behave as $\exp(\pm iky)$ at $y\to\infty$. One can interpret these fundamental solutions at $k\neq 0$ as incident and reflected acoustic waves.

In the inviscid limit, the wave numbers of the fast and slow acoustic waves (α_{FA} and α_{SA}, respectively), can be found analytically as follows:

$$\alpha_{\mathrm{FA}}=\frac{\omega M^2}{M^2-1}-\frac{\sqrt{k^2+\dfrac{\omega^2M^2}{M^2-1}}}{\sqrt{M^2-1}}, \tag{31a}$$

$$\alpha_{\mathrm{SA}}=\frac{\omega M^2}{M^2-1}+\frac{\sqrt{k^2+\dfrac{\omega^2M^2}{M^2-1}}}{\sqrt{M^2-1}}. \tag{31b}$$

At the finite Reynolds number, the wave numbers α_{FA} and α_{SA} are found numerically from the characteristic equation for fundamental solutions outside the boundary layer at prescribed parameter k.[2,3] Figure 20(a) shows dimensionless real parts of α_{FA} and α_{SA} as functions of the parameter k in case 1 corresponding to the frequency 134.28 kHz. Branches of the acoustic spectrum in the complex plane α are presented in Fig. 20(b).

Projection of the computational data onto the eigenfunction system allows evaluation of the amplitudes of the modes and, therefore, a revelation of the underlying physics. Figure 21 shows the computational (input) data for the streamwise velocity perturbation corresponding to the frequency 134.28 kHz in case 1 at $x=x_{\mathrm{data}}$, the reconstructed input of two discrete modes (S and F), and the acoustic modes ("A" stands for sum of the slow and fast acoustic modes). In this example, amplitudes of the modes are determined from the computational results with the help of the orthogonality relation (25). Integrals corresponding to the continuous spectra

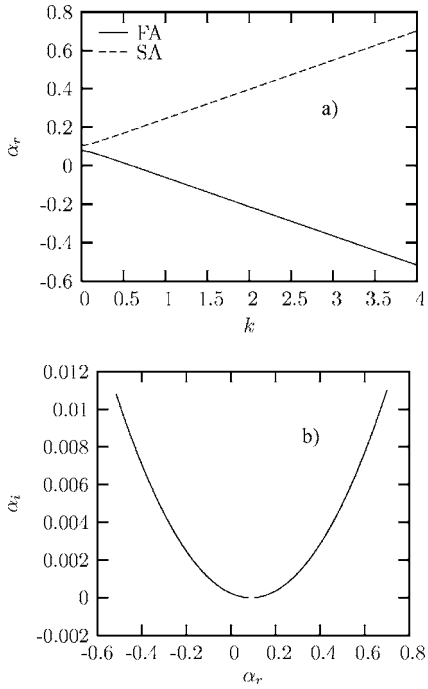

FIG. 20. Streamwise wave numbers of the fast (FA) and slow (SA) acoustic modes, case 1 (134.28 kHz).

in (20) are evaluated numerically with respect to k from 0 to 4 with the help of the trapezoidal formula resulting from 100 steps on the interval. Computations with larger numbers of steps and longer intervals of the integration have not revealed a visible difference on the scale used in Fig. 21.

One can see that the acoustics provides the main input outside the boundary layer. The wiggles in the computational data (at $y/H\approx 35-45$) are associated with the acoustic perturbations emanating from the slot and propagating along the Mach lines outside the boundary layer. In this case, $M\approx 6.62$ and the Mach angle $\mu\approx 8.69^{\circ}$. One can find the width, Δy, of the perturbation strip propagating along the Mach lines as $\Delta y=w\tan\mu\approx 14.7H$, which is in agreement with the results in Fig. 21.

In the inviscid flow, the distance between the wall and the strip is $(x_{\mathrm{data}}-x_c-0.5w)\times\tan\mu\approx 17.25H$. As follows

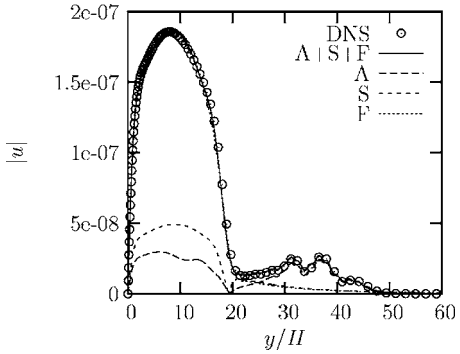

FIG. 21. Input DNS data at $x=x_{\mathrm{data}}$ and results of the projection onto modes of discrete spectrum (S and F), and the acoustic modes, case 1 (134.28 kHz).

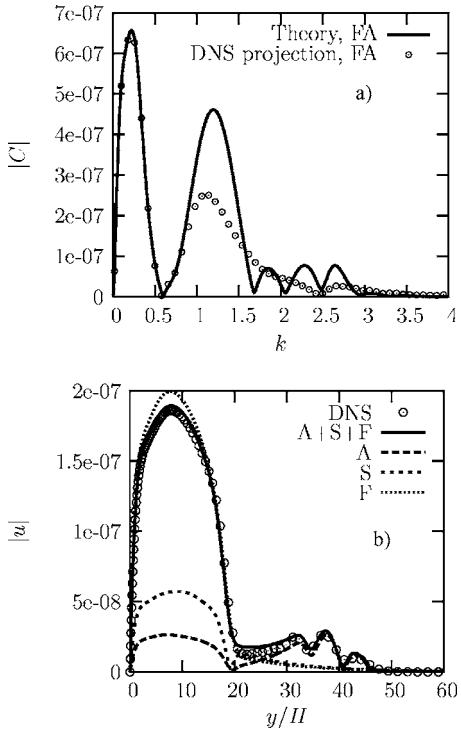

FIG. 22. Amplitudes of the fast acoustic modes (a) and predicted velocity perturbation profiles (b), case 1 (134.28 kHz).

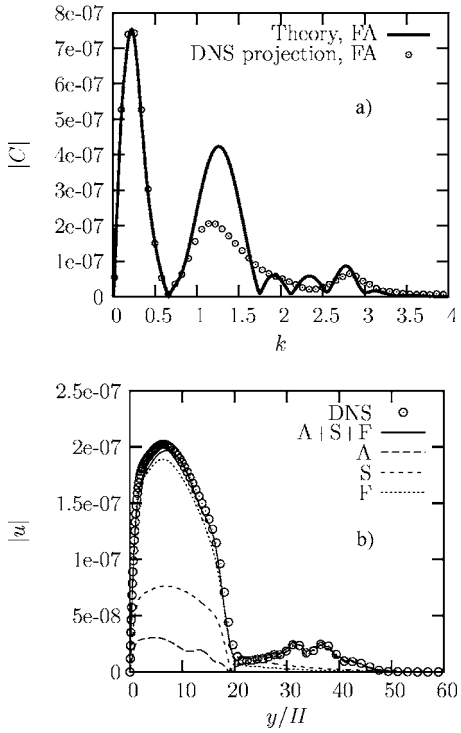

FIG. 23. Amplitudes of the fast acoustic modes (a) and reconstructed velocity perturbation profiles (b), case 1 (149.2 kHz).

from Fig. 21, there is the boundary-layer flow effect, and the strip is displaced from the wall a distance of about δ_{99}.

At the parameters corresponding to the results in Fig. 21, the main input into the perturbation profile inside the boundary layer is associated with the fast (F) discrete mode. It is also found that the slow acoustic modes have small amplitudes in comparison with the fast modes, similar to the previous studies.[7,16]

It is interesting to compare the amplitudes of the acoustic modes obtained with the help of the receptivity problem solution and their amplitudes obtained as a projection of the computational results. Figure 22(a) shows the theoretical amplitudes of the fast acoustic modes and the values filtered out from the computational results. One can see that there is a discrepancy between them at $k \approx 1-1.5$. The discrepancy might be attributed to the grid in the DNS not being fine enough in the vicinity of the wiggles at $y/H \approx 35-45$ having the length scale $\leqslant 2\pi$.

Figures 23–26 show comparisons of the theoretical prediction for amplitudes of the fast acoustic modes and their amplitudes found as a projection of the computational results, together with the reconstructed profiles of the velocity perturbations in case 1 at frequencies 149.2 , 164.12 , 179.04 , and 193.96 kHz, respectively.

V. DISCUSSION OF THE RESULTS

The results of the present work serve as an illustration of how the biorthogonal eigenfunction system can provide an insight into computations. In order to be able to distinguish the modes, one needs amplitude and phase distributions for pressure, temperature, and velocity components, together with some of their derivatives, given at only one station x. The necessary information is always available in computational studies, and the described method allows finding the amplitudes of the modes from the discrete and continuous spectra. For example, the results illustrate how one can find

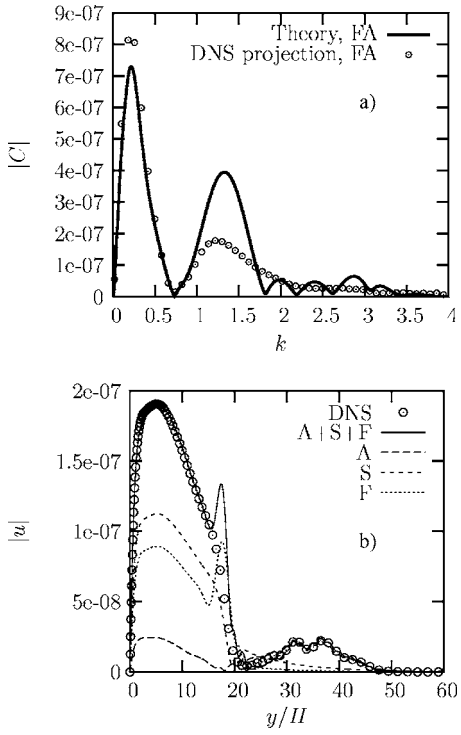

FIG. 24. Amplitudes of the fast acoustic modes (a) and reconstructed velocity perturbation profiles (b), case 1 (164.12 kHz).

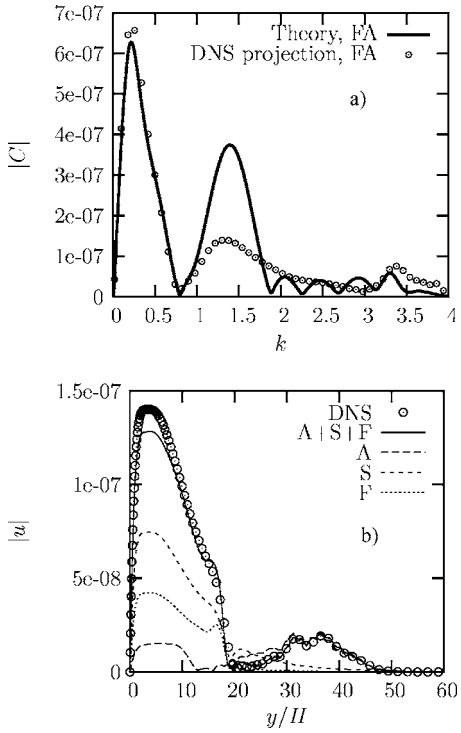

FIG. 25. Amplitudes of the fast acoustic modes (a) and reconstructed velocity perturbation profiles (b), case 1 (179.04 kHz).

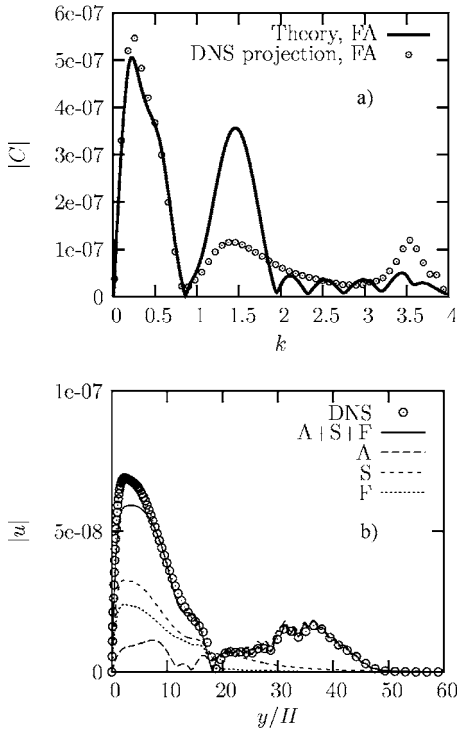

FIG. 26. Amplitudes of the fast acoustic modes (a) and reconstructed velocity perturbation profiles (b), case 1 (193.96 kHz).

amplitudes of the decaying modes in numerical simulations that could not be addressed at all in the past (only unstable modes dominating the perturbation field in a numerical simulation could be compared with predictions of the linear stability theory).

The solution in the present work is based on the parallel flow approximation. This approximation is valid when the characteristic scale of the perturbation (wavelength) is much smaller than the characteristic scale of the unperturbed flow in the downstream direction. This condition is violated when the actuator is located close to the leading edge (see case 3 in Sec. IV). The results of the present work are also based on the assumption that the denominator in (30) is not equal to zero. Fedorov and Khokhlov[24] showed that the denominator is equal to zero at the branching point of two discrete modes. In this case, the nonparallel flow effects are to be taken into account in order to resolve the singularity. Analysis of case 6 ($f \approx 104$ kHz) showed that the denominator tends to zero in the case of synchronism between the discrete mode and the continuous spectra. Therefore, an extension of the theoretical model of Ref. 24 to the case of continuous spectra is required.

Decomposition of perturbations when only partial information is available is an ill-posed problem. Nevertheless, it is still possible to analyze the flow field if some additional information about the data is available. Tumin *et al.*[1–3,9] discussed examples in which the perturbations could be decomposed into the normal modes when only partial information was available. Further development of this approach might be especially helpful in analysis of experimental data in high-speed boundary layers.

ACKNOWLEDGMENTS

This work was sponsored by the Air Force Office of Scientific Research, USAF, under Grants No. FA9550-05-101 (A.T.) and FA9550-04-1-0029 (X.Z. and X.W.) monitored by Dr. J. D. Schmisseur. The views and conclusions contained herein are those of the authors and should not be interpreted as necessarily representing the official policies or endorsements, either expressed or implied, of the Air Force Office of Scientific Research or the U. S. Government.

[1] A. Tumin, "Multimode decomposition of spatially growing perturbations in a two-dimensional boundary layer," Phys. Fluids **15**, 2525 (2003).
[2] P. Guydos and A. Tumin, "Multimode decomposition in compressible boundary layers," AIAA J. **42**, 1115 (2004).
[3] A. Tumin, "Three-dimensional spatial normal modes in compressible boundary layers," AIAA Paper 2006–1109 (2006).
[4] V. N. Zhigulev and A. M. Tumin, *Origin of Turbulence* (Nauka, Novosibirsk, 1987) (in Russian) [NASA TT-20340, October 1988 (translated)].
[5] A. Tumin and E. Reshotko, "The problem of boundary-layer flow encountering a three-dimensional hump revisited," AIAA Paper 2004–0101 (2004).
[6] A. Tumin and E. Reshotko, "Receptivity of a boundary-layer flow to a three-dimensional hump at finite Reynolds numbers," Phys. Fluids **17**, 094101 (2005).
[7] A. Tumin, "Receptivity of compressible boundary layers to three-dimensional wall perturbations," AIAA Paper 2006–1110 (2006).
[8] A. Tumin, "Biorthogonal eigenfunction system in the triple-deck limit," Stud. Appl. Math. **117**, 165 (2006).
[9] A. Tumin, M. Amitay, J. Cohen, and M. Zhou, "A normal multi-mode decomposition method for stability experiments," Phys. Fluids **8**, 2777 (1996).
[10] X. Wang and X. Zhong, "Receptivity of a Mach 8.0 flow over a sharp wedge with half-angle 5.3° to wall blowing-suction," AIAA Paper 2005–5025 (2005).
[11] M. R. Malik, R. S. Lin, and R. Sengupta, "Computation of hypersonic boundary-layer response to external disturbances," AIAA Paper 1999–0411 (1999).

[12] Y. Ma and X. Zhong, "Receptivity to freestream disturbances of Mach 8 flow over a sharp wedge," AIAA Paper 2003–0788 (2003).
[13] X. Zhong, "High-order finite-difference schemes for numerical simulation of hypersonic boundary-layer transition," J. Comput. Phys. **144**, 662 (1998).
[14] A. V. Fedorov, "Excitation of Tollmien-Schlichting waves in a boundary layer by periodic external source located on the body surface," Fluid Dyn. **19**, 888 (1984).
[15] D. Ashpis and E. Reshotko, "The vibrating ribbon problem revisited," J. Fluid Mech. **213**, 531 (1990).
[16] P. Balakumar and M. R. Malik, "Discrete modes and continuous spectra in supersonic boundary layer," J. Fluid Mech. **239**, 631 (1992).
[17] A. M. Tumin and A. V. Fedorov, "Spatial growth of disturbances in a compressible boundary layer," J. Appl. Mech. Tech. Phys. **24**, 548 (1983).
[18] A. Fedorov and A. Tumin, "Initial-value problem for hypersonic boundary layer flows," AIAA J. **41**, 379 (2003).
[19] A. V. Fedorov and A. P. Khokhlov, "Mode switching in a supersonic boundary layer," J. Appl. Mech. Tech. Phys. **32**, 831 (1991).
[20] A. V. Fedorov and A. P. Khokhlov, "Prehistory of instability in a hypersonic boundary layer," Theor. Comput. Fluid Dyn. **14**, 359 (2001).
[21] Y. Ma and X. Zhong, "Receptivity of a supersonic boundary layer over a flat plate. Part 2: Receptivity to freestream sound," J. Fluid Mech. **488**, 79 (2003).
[22] M. Choudhari, "Distributed acoustic receptivity in laminar flow control configurations," Phys. Fluids **6**, 489 (1994).
[23] F. B. Bertolotti, "Receptivity of three-dimensional boundary-layers to localized wall roughness and suction," Phys. Fluids **12**, 1799 (2000).
[24] A. V. Fedorov and A. P. Khokhlov, "Receptivity of hypersonic boundary layer to wall disturbances," Theor. Comput. Fluid Dyn. **15**, 231 (2002).